

# First search for the weak radiative decays $\Lambda_c^+ \rightarrow \Sigma^+ \gamma$ and $\Xi_c^0 \rightarrow \Xi^0 \gamma$

(The Belle Collaboration)

We present the first search for the weak radiative decays  $\Lambda_c^+ \rightarrow \Sigma^+ \gamma$  and  $\Xi_c^0 \rightarrow \Xi^0 \gamma$  using a data sample of  $980 \text{ fb}^{-1}$  collected by the Belle detector operating at the KEKB asymmetric-energy  $e^+e^-$  collider. There are no evident  $\Lambda_c^+ \rightarrow \Sigma^+ \gamma$  or  $\Xi_c^0 \rightarrow \Xi^0 \gamma$  signals. Taking the decays  $\Lambda_c^+ \rightarrow pK^-\pi^+$  and  $\Xi_c^0 \rightarrow \Xi^-\pi^+$  as normalization channels, the upper limits at 90% credibility level on the ratios of branching fractions  $\mathcal{B}(\Lambda_c^+ \rightarrow \Sigma^+ \gamma)/\mathcal{B}(\Lambda_c^+ \rightarrow pK^-\pi^+) < 4.0 \times 10^{-3}$  and  $\mathcal{B}(\Xi_c^0 \rightarrow \Xi^0 \gamma)/\mathcal{B}(\Xi_c^0 \rightarrow \Xi^-\pi^+) < 1.2 \times 10^{-2}$  are determined. We obtain the upper limits at 90% credibility level on the absolute branching fractions  $\mathcal{B}(\Lambda_c^+ \rightarrow \Sigma^+ \gamma) < 2.6 \times 10^{-4}$  and  $\mathcal{B}(\Xi_c^0 \rightarrow \Xi^0 \gamma) < 1.8 \times 10^{-4}$ .

## I. INTRODUCTION

Charm physics has always been a popular topic due to the fact that the charm system provides a distinctive laboratory to investigate the interplay of strong and weak interactions. Weak radiative decays of charmed hadrons proceed via  $W$ -exchange, and are dominated by long-distance nonperturbative processes; short-distance contributions from electromagnetic penguin diagrams are highly suppressed [1, 2]. The long-distance contributions to the Cabibbo-favored (CF) weak radiative decays of charmed hadrons are predicted to have branching fractions at the level of  $10^{-4}$  [1–8]. Measurements of the branching fractions of weak radiative decays of charmed hadrons can be used to test long-distance dynamics calculations based on different theoretical models.

In the charmed meson sector, several weak radiative decays have been reported [9–11]. The Cabibbo-suppressed (CS) weak radiative decay  $D^0 \rightarrow \phi \gamma$  was first observed by the Belle experiment [9]. The BABAR experiment found the CF weak radiative decay  $D^0 \rightarrow \bar{K}^*(892)^0 \gamma$  [10]. In 2017, the Belle experiment presented the first observation of the CS weak radiative decay  $D^0 \rightarrow \rho^0 \gamma$  with a measured branching fraction  $\mathcal{B}(D^0 \rightarrow \rho^0 \gamma) = (1.77 \pm 0.30 \pm 0.07) \times 10^{-5}$  and the improved measurements of branching fractions  $\mathcal{B}(D^0 \rightarrow \phi \gamma) = (2.76 \pm 0.19 \pm 0.10) \times 10^{-5}$  and  $\mathcal{B}(D^0 \rightarrow \bar{K}^*(892)^0 \gamma) = (4.66 \pm 0.21 \pm 0.21) \times 10^{-4}$  [11], where the first and second uncertainties are statistical and systematic, respectively. However, the weak radiative decays of charmed baryons have not yet been measured.

The LHCb experiment observed the first weak radiative decay of a bottom baryon  $\Lambda_b^0 \rightarrow \Lambda \gamma$  in 2019, and measured the branching fraction  $\mathcal{B}(\Lambda_b^0 \rightarrow \Lambda \gamma) = (7.1 \pm 1.5 \pm 0.6 \pm 0.7) \times 10^{-6}$ , where the quoted uncertainties are statistical, systematic, and from the external inputs, respectively [12]. The decay  $\Lambda_b^0 \rightarrow \Lambda \gamma$  proceeds via the  $b \rightarrow s \gamma$  flavor-changing neutral-current transition, which is dominated by short-distance processes. Since the penguin process  $c \rightarrow u \gamma$  is highly suppressed, it plays very little role in the weak radiative decays of charmed baryons. More dominant contributions to the weak radiative decays of charmed baryons could arise from  $W$ -exchange bremsstrahlung processes such as  $cd \rightarrow us \gamma$ .

The  $cd \rightarrow us \gamma$  process induces two CF weak radiative decays of anti-triplet charmed baryons:  $\Lambda_c^+ \rightarrow \Sigma^+ \gamma$  and  $\Xi_c^0 \rightarrow \Xi^0 \gamma$  [13]. Figure 1 shows the  $W$ -exchange diagrams accompanied by a photon emission from the external  $s$  quark for  $\Lambda_c^+ \rightarrow \Sigma^+ \gamma$  and  $\Xi_c^0 \rightarrow \Xi^0 \gamma$  decays as examples. The same  $W$ -exchange diagrams, but with a photon radiated from other external quarks, can also contribute to the weak radiative decays  $\Lambda_c^+ \rightarrow \Sigma^+ \gamma$  and  $\Xi_c^0 \rightarrow \Xi^0 \gamma$  [4]. The branching fractions of the decays  $\Lambda_c^+ \rightarrow \Sigma^+ \gamma$  and  $\Xi_c^0 \rightarrow \Xi^0 \gamma$  were predicted by the different theoretical methods, including a modified nonrelativistic quark model [4], the constituent quark model [5], and the effective Lagrangian approach [6]. Theoretical branching fraction estimates cover ranges of  $(4.5 - 29.1) \times 10^{-5}$  and  $(3.0 - 19.5) \times 10^{-5}$  for  $\Lambda_c^+ \rightarrow \Sigma^+ \gamma$  and  $\Xi_c^0 \rightarrow \Xi^0 \gamma$  decays [4–6], respectively, as listed in Table I. There are two estimates in Ref. [5], and the case (II) naively considered the flavor dependence of charmed baryon wave-function squared at the origin  $|\psi(0)|^2$ . Very recently, the authors of Ref. [14] propose a new method of self-analyzing final states to test the standard model and search for possible new physics (NP) in the radiative decays of charmed baryons. Measuring the branching fractions of weak radiative decays  $\Lambda_c^+ \rightarrow \Sigma^+ \gamma$  and  $\Xi_c^0 \rightarrow \Xi^0 \gamma$  can not only exclude the parameter space of NP existence but also yield experimental inputs for the theoretical understanding of long-distance interactions in the weak radiative decays of charmed hadrons.

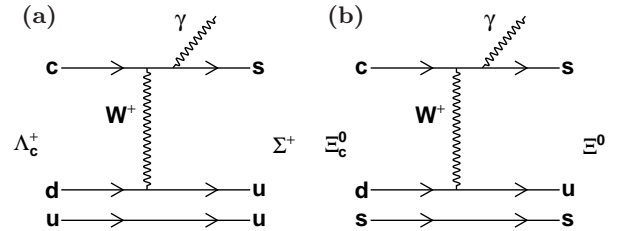


FIG. 1: Examples of  $W$ -exchange diagrams accompanied by photon emission from the external  $s$  quark for (a)  $\Lambda_c^+ \rightarrow \Sigma^+ \gamma$  and (b)  $\Xi_c^0 \rightarrow \Xi^0 \gamma$  decays.

In this paper, we perform the first search for the weak radiative decays  $\Lambda_c^+ \rightarrow \Sigma^+ \gamma$  and  $\Xi_c^0 \rightarrow \Xi^0 \gamma$  using the entire data sample of  $980 \text{ fb}^{-1}$  collected by the

TABLE I: Theoretical estimates of branching fractions in units of  $10^{-5}$  for the CF weak radiative decays  $\Lambda_c^+ \rightarrow \Sigma^+\gamma$  and  $\Xi_c^0 \rightarrow \Xi^0\gamma$ . There are two predictions in Ref. [5] depending on the evaluation of the charmed baryon wave-function squared at the origin  $|\psi(0)|^2$ . The branching fractions have been rescaled based on the current lifetimes of  $\Lambda_c^+$  and  $\Xi_c^0$  by the author of Ref. [13].

Modes	Kamal [4]	Uppal [5]		Cheng [6]
		(I)	(II)	
$\Lambda_c^+ \rightarrow \Sigma^+\gamma$	6.0	4.5	29.1	4.9
$\Xi_c^0 \rightarrow \Xi^0\gamma$	...	3.0	19.5	4.8

Belle detector. The decays  $\Lambda_c^+ \rightarrow pK^-\pi^+$  and  $\Xi_c^0 \rightarrow \Xi^-\pi^+$  are taken as normalization channels. Charge-conjugate modes are also implied unless otherwise stated throughout this paper.

## II. THE DATA SAMPLE AND THE BELLE DETECTOR

This analysis is based on data collected at or near the  $\Upsilon(nS)$  ( $n = 1, 2, 3, 4, 5$ ) resonances by the Belle detector [15, 16] at the KEKB asymmetric-energy  $e^+e^-$  collider [17, 18]. The total data sample corresponds to an integrated luminosity of  $980 \text{ fb}^{-1}$  [16]. The Belle detector is a large-solid-angle magnetic spectrometer consisting of a silicon vertex detector, a 50-layer central drift chamber (CDC), an array of aerogel threshold Cherenkov counters (ACC), a barrel-like arrangement of time-of-flight scintillation counters (TOF), and an electromagnetic calorimeter comprising CsI(Tl) crystals (ECL) located inside a superconducting solenoid coil that provides a 1.5 T magnetic field. An iron flux return comprising resistive plate chambers located outside the coil is instrumented to detect  $K_L^0$  mesons and to identify muons. The detector is described in detail elsewhere [15, 16].

Monte Carlo (MC) simulated signal events are generated using EVTGEN [19] to optimize the signal selection criteria and calculate the reconstruction efficiencies. Events for the  $e^+e^- \rightarrow c\bar{c}$  production are generated using PYTHIA [20] with a specific Belle configuration, where one of the two charm quarks hadronizes into a  $\Lambda_c^+$  or  $\Xi_c^0$  baryon. The decays  $\Lambda_c^+ \rightarrow \Sigma^+\gamma$ ,  $\Xi_c^0 \rightarrow \Xi^0\gamma$ ,  $\Lambda_c^+ \rightarrow pK^-\pi^+$ ,  $\Xi_c^0 \rightarrow \Xi^-\pi^+$ ,  $\Lambda_c^+ \rightarrow \Sigma^+\pi^0$ ,  $\Lambda_c^+ \rightarrow \Sigma^+\eta$ ,  $\Xi_c^0 \rightarrow \Xi^0\pi^0$ , and  $\Xi_c^0 \rightarrow \Xi^0\eta$  are generated using a phase space model. The simulated events are processed with a detector simulation based on GEANT3 [21]. Inclusive MC samples of  $\Upsilon(1S, 2S, 3S)$  decays,  $\Upsilon(4S) \rightarrow B^+B^-/B^0\bar{B}^0$ ,  $\Upsilon(5S) \rightarrow B_{(s)}^{(*)}\bar{B}_{(s)}^{(*)}$ , and  $e^+e^- \rightarrow q\bar{q}$  ( $q = u, d, s, c$ ) at center-of-mass (C.M.) energies of 9.460, 10.024, 10.355, 10.520, 10.580, and 10.867 GeV corresponding to two times the integrated luminosity of data are used to check for possible peaking

backgrounds and optimize the signal selection criteria.

## III. COMMON EVENT SELECTION CRITERIA

We reconstruct the decays  $\Lambda_c^+ \rightarrow \Sigma^+\gamma$ ,  $\Xi_c^0 \rightarrow \Xi^0\gamma$ ,  $\Lambda_c^+ \rightarrow pK^-\pi^+$ , and  $\Xi_c^0 \rightarrow \Xi^-\pi^+$ . The  $\Sigma^+$ ,  $\Xi^0$ , and  $\Xi^-$  hyperons are reconstructed via  $\Sigma^+ \rightarrow p\pi^0$ ,  $\Xi^0 \rightarrow \Lambda\pi^0$ , and  $\Xi^- \rightarrow \Lambda\pi^-$  decays with the  $\pi^0$  and  $\Lambda$  in  $\pi^0 \rightarrow \gamma\gamma$  and  $\Lambda \rightarrow p\pi^-$  decays, respectively. The event selection criteria described below are optimized by maximizing the figure-of-merit  $\epsilon/(3/2 + \sqrt{N_{\text{bkg}}})$  [22], where  $\epsilon$  is the signal reconstruction efficiency of  $\Lambda_c^+ \rightarrow \Sigma^+\gamma$  or  $\Xi_c^0 \rightarrow \Xi^0\gamma$  decay, and  $N_{\text{bkg}}$  is the number of estimated background events from the normalized inclusive MC samples in the  $\Lambda_c^+$  or  $\Xi_c^0$  signal region defined as  $2.18 \text{ GeV}/c^2 < M(\Sigma^+\gamma) < 2.34 \text{ GeV}/c^2$  or  $2.36 \text{ GeV}/c^2 < M(\Xi^0\gamma) < 2.52 \text{ GeV}/c^2$  ( $> 95\%$  signal events are retained according to signal MC simulations), respectively. Hereinafter,  $M$  represents the measured invariant mass.

For the particle identification (PID) of a well-reconstructed charged track, information from different detector subsystems, including specific ionization in the CDC, time measurement in the TOF, and the response of the ACC, is combined to form a likelihood ratio,  $\mathcal{R}(h|h') = \mathcal{L}(h)/[\mathcal{L}(h) + \mathcal{L}(h')]$ , where  $\mathcal{L}(h^{(i)})$  is the likelihood of the charged track being a hadron  $h^{(i)}$ , and  $h^{(i)}$  is  $p$ ,  $K$ , or  $\pi$  as appropriate [23]. To identify the proton used in  $\Sigma^+$  reconstruction, we require  $\mathcal{R}(p|K) > 0.6$  and  $\mathcal{R}(p|\pi) > 0.6$ , which has an efficiency of 97%; we also require a momentum above 0.9 GeV/ $c$  in the laboratory frame. For the proton used in  $\Lambda$  reconstruction, we require  $\mathcal{R}(p|K) > 0.2$  and  $\mathcal{R}(p|\pi) > 0.2$  with an efficiency of 98%.

An ECL cluster is taken as a photon candidate if it does not match the extrapolation of any charged track. The  $\pi^0$  candidates used in  $\Sigma^+$  ( $\Xi^0$ ) reconstruction are formed from two photons having energy exceeding 50 MeV (30 MeV) in the barrel ( $-0.63 < \cos\theta < 0.85$ ) or 70 MeV (50 MeV) in the endcaps ( $-0.91 < \cos\theta < -0.63$  or  $0.85 < \cos\theta < 0.98$ ) of the ECL, where  $\theta$  is the polar angle relative to the opposite direction of  $e^+$  beam. The reconstructed invariant mass of the  $\pi^0$  candidate is required to be within 10.8 MeV/ $c^2$  of the  $\pi^0$  nominal mass [24], corresponding to approximately twice the mass resolution ( $\sigma$ ). To reduce the large combinatorial backgrounds, the momentum of the  $\pi^0$  used in  $\Sigma^+$  ( $\Xi^0$ ) reconstruction is required to exceed 300 MeV/ $c$  (200 MeV/ $c$ ) in the laboratory frame. The  $\Lambda$  candidates are reconstructed in the decay  $\Lambda \rightarrow p\pi^-$  and selected if  $|M(p\pi^-) - m(\Lambda)| < 3.5 \text{ MeV}/c^2$  ( $\sim 2.5\sigma$ ). Here and throughout this paper,  $m(i)$  represents the nominal mass of the particle  $i$  [24].

The  $\Sigma^+ \rightarrow p\pi^0$  and  $\Xi^0 \rightarrow \Lambda\pi^0$  reconstructions are complicated by the fact that the parent hyperon decays with a  $\pi^0$ , which has negligible vertex position

information, as one of its daughters. For the  $\Sigma^+ \rightarrow p\pi^0$  reconstruction, combinations of  $\pi^0$  candidates and protons are made using those protons with a sufficiently large ( $> 1$  mm) distance of closest approach to the interaction point (IP). Then, taking the IP as the point of origin of the  $\Sigma^+$ , the sum of the proton and  $\pi^0$  momenta is taken as the momentum vector of the  $\Sigma^+$  candidate. The intersection of this trajectory with the reconstructed proton trajectory is then found and this position is taken as the decay location of the  $\Sigma^+$  hyperon. The  $\pi^0$  is then re-made from the two photons, using this location as its point of origin. Only those combinations with the decay location of the  $\Sigma^+$  indicating a positive  $\Sigma^+$  path length are retained. The  $\Xi^0 \rightarrow \Lambda\pi^0$  decays are reconstructed using a similar method, and only those combinations with the decay location of the  $\Xi^0$  indicating a positive  $\Xi^0$  path length of greater than 2 cm but less than the distance between the  $\Lambda$  decay vertex and the IP are retained [25].

The following criteria are used to select the radiative photon candidates. The energy of the photon is required to exceed 0.65 GeV in the barrel or 0.8 GeV in the endcaps of the ECL. To reduce photon candidates originating from neutral hadrons, we reject a photon candidate if the ratio of energy deposited in the central  $3 \times 3$  square of cells to that deposited in the enclosing  $5 \times 5$  square of cells in its ECL cluster is less than 0.95. Most background photons originate from  $\pi^0 \rightarrow \gamma\gamma$  and  $\eta \rightarrow \gamma\gamma$  decays. To reduce such backgrounds, probability functions are employed to distinguish the radiative photon candidates from  $\pi^0$  and  $\eta$  decays. We first combine the photon candidate with all other photons and calculate likelihoods for the reconstructed photon pair to be  $\pi^0$ -like [ $\mathcal{P}(\pi^0)$ ] and  $\eta$ -like [ $\mathcal{P}(\eta)$ ], by using the invariant mass of the photon pair along with the energy of the candidate photon in the laboratory frame and the angle with respect to the beam direction in the laboratory frame [26]. The background photons originating from  $\pi^0 \rightarrow \gamma\gamma$  and  $\eta \rightarrow \gamma\gamma$  decays are suppressed by requiring  $\mathcal{P}(\pi^0) < 0.3$  and  $\mathcal{P}(\eta) < 0.3$ .

The  $\Sigma^+\gamma$  and  $\Xi^0\gamma$  combinations are made to form  $\Lambda_c^+$  and  $\Xi_c^0$  candidates, respectively. To reduce the combinatorial backgrounds, especially from  $B$ -meson decays, the scaled momentum  $x_p = p_i^*/p_{\max}$  is required to be larger than 0.55. Here,  $p_i^*$  is the momentum of the  $\Lambda_c^+$  or  $\Xi_c^0$  candidate in the  $e^+e^-$  C.M. frame, and  $p_{\max} = \frac{1}{c}\sqrt{E_{\text{beam}}^2 - M_i^2 c^4}$ , where  $E_{\text{beam}}$  is the beam energy in the  $e^+e^-$  C.M. frame and  $M_i$  represents the invariant mass of the  $\Lambda_c^+$  or  $\Xi_c^0$  candidate.

For the normalization channels  $\Lambda_c^+ \rightarrow pK^-\pi^+$  and  $\Xi_c^0 \rightarrow \Xi^-\pi^+$ , the selection criteria are similar to those used in Refs. [27, 28] and are described below. For the  $\Lambda_c^+ \rightarrow pK^-\pi^+$  reconstruction, tracks having  $\mathcal{R}(p|K) > 0.9$  and  $\mathcal{R}(p|\pi) > 0.9$  are identified as proton candidates; charged kaon candidates are required to have  $\mathcal{R}(K|\pi) > 0.9$  and  $\mathcal{R}(K|p) > 0.4$ ; and charged pion candidates to have  $\mathcal{R}(\pi|K) > 0.4$  and  $\mathcal{R}(\pi|p) > 0.4$ . A likelihood ratio for electron identification,  $\mathcal{R}(e)$ , is formed from ACC,

CDC, and ECL information [29], and is required to be less than 0.9 for all charged tracks to suppress electrons. For each charged track, the impact parameters with respect to the IP are required to be less than 0.1 cm and 2.0 cm perpendicular to, and along the  $e^+$  beam direction, respectively. The  $\Lambda_c^+$  candidate is reconstructed by combining  $p$ ,  $K^-$ , and  $\pi^+$  candidates. A vertex fit is performed for the reconstructed  $\Lambda_c^+$  candidate with a requirement of  $\chi_{\text{vertex}}^2 < 40$ . The required  $x_p$  value of  $\Lambda_c^+ \rightarrow pK^-\pi^+$  is the same as that of corresponding signal channel.

For the  $\Xi_c^0 \rightarrow \Xi^-\pi^+$  reconstruction, tracks having  $\mathcal{R}(\pi|K) > 0.6$  and  $\mathcal{R}(\pi|p) > 0.6$  are identified as pion candidates. For the  $\pi^+$  that is the direct daughter of the  $\Xi_c^0$ , the impact parameters with respect to the IP are required to be less than 0.5 cm and 4.0 cm perpendicular to, and along the  $e^+$  beam direction, respectively, and the transverse momentum is restricted to be higher than 0.1 GeV/ $c$ . The  $\Lambda$  candidates are selected using the same procedure as in the signal channel. The  $\Xi^-$  candidates are reconstructed from the combinations of selected  $\Lambda$  and  $\pi^-$  candidates. We define the  $\Xi^-$  signal region as  $|M(\Lambda\pi^-) - m(\Xi^-)| < 6.5$  MeV/ $c^2$  ( $\sim 3.0\sigma$ ). Finally, the reconstructed  $\Xi^-$  candidate is combined with a  $\pi^+$  to form the  $\Xi_c^0$  candidate. We perform vertex fits for the  $\Lambda$ ,  $\Xi^-$ , and  $\Xi_c^0$  candidates. To suppress the combinatorial backgrounds, we require the flight directions of  $\Lambda$  and  $\Xi^-$  candidates, which are reconstructed from their fitted production and decay vertices, to be within  $5^\circ$  of their momentum directions. The requirement on  $x_p$  value of  $\Xi_c^0 \rightarrow \Xi^-\pi^+$  is the same as that of the corresponding signal channel.

#### IV. EXTRACTIONS OF $\Lambda_c^+ \rightarrow \Sigma^+\gamma$ AND $\Xi_c^0 \rightarrow \Xi^0\gamma$ SIGNAL YIELDS

The  $M(pK^-\pi^+)$  and  $M(\Xi^-\pi^+)$  distributions of events corresponding to the normalization channels  $\Lambda_c^+ \rightarrow pK^-\pi^+$  and  $\Xi_c^0 \rightarrow \Xi^-\pi^+$  in data are shown in Figs. 2(a) and 2(b), respectively. To extract the  $\Lambda_c^+ \rightarrow pK^-\pi^+$  and  $\Xi_c^0 \rightarrow \Xi^-\pi^+$  signal yields, we perform binned extended maximum-likelihood fits to the  $M(pK^-\pi^+)$  and  $M(\Xi^-\pi^+)$  distributions. In the fits, double-Gaussian functions are taken as the signal probability density functions (PDFs) for the  $\Lambda_c^+$  and  $\Xi_c^0$ , and the combinatorial background PDFs are parametrized by a second-order polynomial for the  $M(pK^-\pi^+)$  distribution and a first-order polynomial for  $M(\Xi^-\pi^+)$ . The parameters of the signal and combinatorial background PDFs are free. The fitted results are displayed in Fig. 2 along with the distributions of the pulls  $(N_{\text{data}} - N_{\text{fit}})/\sigma_{\text{data}}$ , where  $\sigma_{\text{data}}$  is the uncertainty on  $N_{\text{data}}$ , and the fitted signal yields of  $\Lambda_c^+ \rightarrow pK^-\pi^+$  and  $\Xi_c^0 \rightarrow \Xi^-\pi^+$  decays in data are  $(1281910 \pm 2040)$  and  $(45063 \pm 445)$ , respectively.

For the three-body decay  $\Lambda_c^+ \rightarrow pK^-\pi^+$ , the

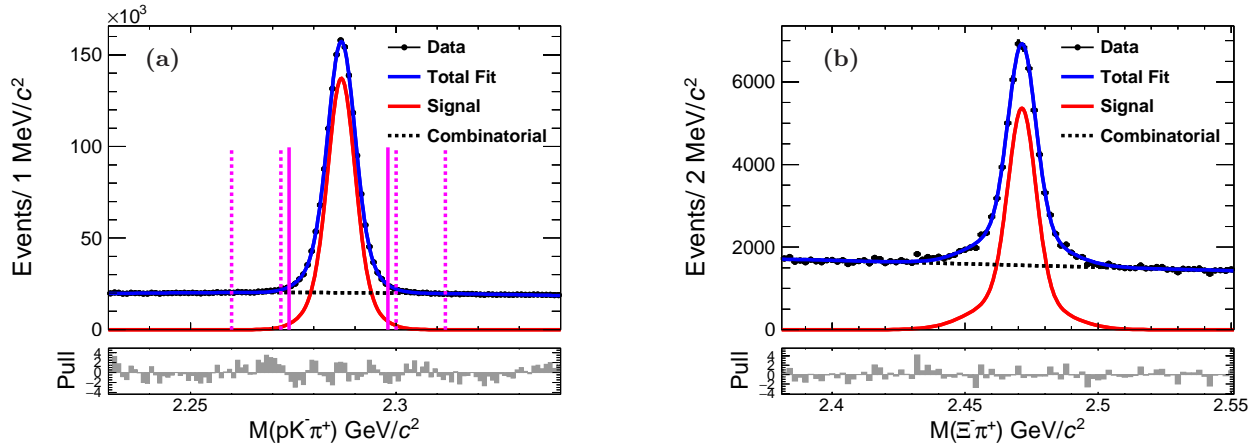


FIG. 2: The invariant mass distributions of (a)  $pK^-\pi^+$  and (b)  $\Xi^-\pi^+$  from the reconstructed  $\Lambda_c^+ \rightarrow pK^-\pi^+$  and  $\Xi_c^0 \rightarrow \Xi^-\pi^+$  candidates in data. The points with error bars represent the data, the blue solid curves show the best-fit results, the red solid curves denote the fitted signals, and the black dashed curves represent the fitted combinatorial backgrounds. In (a), the pink solid lines indicate the required signal region, and the pink dashed lines denote the defined sideband regions.

reconstruction efficiency can vary across the phase space, as visualized in a Dalitz distribution [30]. Figure 3 shows the Dalitz distribution of  $M^2(pK^-)$  versus  $M^2(K^-\pi^+)$  from data in the  $\Lambda_c^+$  signal region with the normalized  $\Lambda_c^+$  mass sidebands subtracted. The signal region of  $\Lambda_c^+$  is defined as  $2.274 \text{ GeV}/c^2 < M(pK^-\pi^+) < 2.298 \text{ GeV}/c^2$ , and the sideband regions are defined as  $2.260 \text{ GeV}/c^2 < M(pK^-\pi^+) < 2.272 \text{ GeV}/c^2$  or  $2.300 \text{ GeV}/c^2 < M(pK^-\pi^+) < 2.312 \text{ GeV}/c^2$ . We divide the Dalitz distribution into  $120 \times 120$  bins, with a bin size of  $0.027 \text{ GeV}^2/c^4$  for  $M^2(pK^-)$  and  $0.016 \text{ GeV}^2/c^4$  for  $M^2(K^-\pi^+)$ . The reconstruction efficiency averaged over the Dalitz distribution is calculated by the formula  $\epsilon = \sum_i s_i / \sum_j (s_j / \epsilon_j)$  [27], where  $i$  and  $j$  run over all bins;  $s_{i/j}$  and  $\epsilon_j$  are the number of signal events in data and the reconstruction efficiency from signal MC simulation for each bin, respectively. The reconstruction efficiency for each bin is obtained by dividing the number of signal events after applying the selection criteria with the normalized sidebands subtracted by the number of generated events. The corrected reconstruction efficiency for  $\Lambda_c^+ \rightarrow pK^-\pi^+$  is determined to be  $(12.79 \pm 0.02)\%$ . For the two-body decay  $\Xi_c^0 \rightarrow \Xi^-\pi^+$ , we estimate the reconstruction efficiency directly from the simulated events by the ratio  $n_{\text{sel}}/n_{\text{gen}}$ , where  $n_{\text{sel}}$  and  $n_{\text{gen}}$  are the numbers of true signal events surviving the selection criteria and generated events, respectively. The signal reconstruction efficiency for  $\Xi_c^0 \rightarrow \Xi^-\pi^+$  is determined to be  $(16.96 \pm 0.05)\%$ .

After applying the event selection criteria mentioned in Sec. III, the invariant mass distributions of  $p\pi^0$  and  $\Lambda\pi^0$  from the reconstructed  $\Lambda_c^+ \rightarrow \Sigma^+\gamma$  and  $\Xi_c^0 \rightarrow \Xi^0\gamma$  candidates in data are shown in Figs. 4(a) and 4(b), respectively. There are significant  $\Sigma^+$  and  $\Xi^0$  signals observed in the  $\Lambda_c^+$  and  $\Xi_c^0$  signal regions,

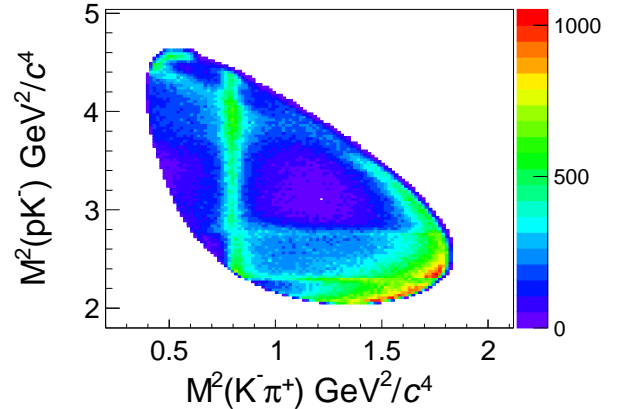


FIG. 3: Dalitz distribution of the reconstructed  $\Lambda_c^+ \rightarrow pK^-\pi^+$  candidates in data.

respectively. The signal regions of  $\Sigma^+$  and  $\Xi^0$  candidates are defined as  $|M(p\pi^0) - m(\Sigma^+)| < 14 \text{ MeV}/c^2$  ( $\sim 2.5\sigma$ ) and  $|M(\Lambda\pi^0) - m(\Xi^0)| < 9 \text{ MeV}/c^2$  ( $\sim 2.5\sigma$ ). We define the  $\Sigma^+$  and  $\Xi^0$  sideband regions as  $1.140 \text{ GeV}/c^2 < M(p\pi^0) < 1.168 \text{ GeV}/c^2$  or  $1.210 \text{ GeV}/c^2 < M(p\pi^0) < 1.238 \text{ GeV}/c^2$ , and  $1.284 \text{ GeV}/c^2 < M(\Lambda\pi^0) < 1.302 \text{ GeV}/c^2$  or  $1.327 \text{ GeV}/c^2 < M(\Lambda\pi^0) < 1.345 \text{ GeV}/c^2$ , respectively, which are twice as wide as the corresponding signal regions. The blue solid lines indicate the required  $\Sigma^+$  and  $\Xi^0$  signal regions, and the blue dashed lines represent the defined  $\Sigma^+$  and  $\Xi^0$  sideband regions.

Figures 5(a) and 5(b) display the invariant mass spectra of  $\Sigma^+\gamma$  and  $\Xi^0\gamma$  from data, and the cyan

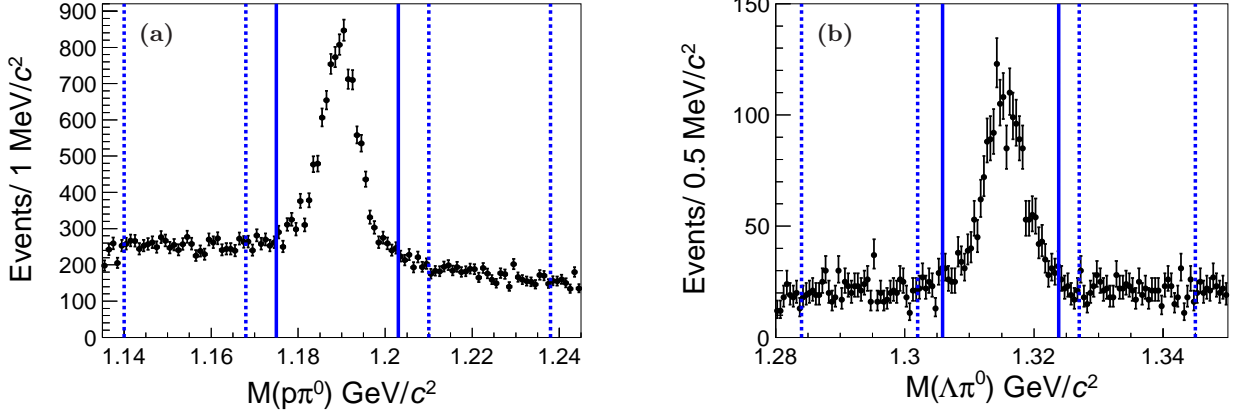


FIG. 4: The invariant mass distributions of (a)  $p\pi^0$  and (b)  $\Lambda\pi^0$  from the reconstructed  $\Lambda_c^+ \rightarrow \Sigma^+\gamma$  and  $\Xi_c^0 \rightarrow \Xi^0\gamma$  candidates in the  $\Lambda_c^+$  and  $\Xi_c^0$  signal regions in data, respectively. The points with error bars represent the data, the blue solid lines indicate the required signal regions, and the blue dashed lines denote the defined sidebands.

shaded histograms represent events from the normalized  $\Sigma^+$  and  $\Xi^0$  sidebands, respectively. There are broad peaking backgrounds found in both  $M(\Sigma^+\gamma)$  and  $M(\Xi^0\gamma)$  distributions in data and inclusive MC samples. According to a study of inclusive MC samples using the TopoAna package [31], we found that these peaking backgrounds in the  $M(\Sigma^+\gamma)$  and  $M(\Xi^0\gamma)$  distributions arise from the contributions of  $\Lambda_c^+ \rightarrow \Sigma^+\pi^0(\rightarrow \gamma\gamma)$  and  $\Sigma^+\eta(\rightarrow \gamma\gamma)$ , and  $\Xi_c^0 \rightarrow \Xi^0\pi^0(\rightarrow \gamma\gamma)$  and  $\Xi^0\eta(\rightarrow \gamma\gamma)$  decays respectively, where one of the two photons has been missed.

For the  $\Lambda_c^+ \rightarrow \Sigma^+\gamma$  mode, the expected peaking background events from the contributions of  $\Lambda_c^+ \rightarrow \Sigma^+\pi^0(\rightarrow \gamma\gamma)$  and  $\Lambda_c^+ \rightarrow \Sigma^+\eta(\rightarrow \gamma\gamma)$  in the  $M(\Sigma^+\gamma)$  distribution are estimated according to the formulae

$$N_{\Sigma^+\pi^0}^{\Sigma^+\gamma} = \varepsilon_{\Sigma^+\pi^0}^{\Sigma^+\gamma} \times \frac{N_{pK^-\pi^+}^{\text{obs}} \mathcal{B}(\Lambda_c^+ \rightarrow \Sigma^+\pi^0)}{\varepsilon_{pK^-\pi^+}} \times \frac{\mathcal{B}(\Sigma^+ \rightarrow p\pi^0)\mathcal{B}(\pi^0 \rightarrow \gamma\gamma)\mathcal{B}(\pi^0 \rightarrow \gamma\gamma)}{\mathcal{B}(\Lambda_c^+ \rightarrow pK^-\pi^+)}$$

and

$$N_{\Sigma^+\eta}^{\Sigma^+\gamma} = \varepsilon_{\Sigma^+\eta}^{\Sigma^+\gamma} \times \frac{N_{pK^-\pi^+}^{\text{obs}} \mathcal{B}(\Lambda_c^+ \rightarrow \Sigma^+\eta)}{\varepsilon_{pK^-\pi^+}} \times \frac{\mathcal{B}(\Sigma^+ \rightarrow p\pi^0)\mathcal{B}(\eta \rightarrow \gamma\gamma)\mathcal{B}(\pi^0 \rightarrow \gamma\gamma)}{\mathcal{B}(\Lambda_c^+ \rightarrow pK^-\pi^+)},$$

where  $\varepsilon_{\Sigma^+\pi^0}^{\Sigma^+\gamma} = 0.36\%$  and  $\varepsilon_{\Sigma^+\eta}^{\Sigma^+\gamma} = 0.46\%$  are the reconstruction efficiencies of  $\Lambda_c^+ \rightarrow \Sigma^+\pi^0(\rightarrow \gamma\gamma)$  and  $\Lambda_c^+ \rightarrow \Sigma^+\eta(\rightarrow \gamma\gamma)$  decays under the  $\Lambda_c^+ \rightarrow \Sigma^+\gamma$  selection criteria obtained by signal MC simulations;  $\varepsilon_{pK^-\pi^+} = (12.79 \pm 0.02)\%$  denotes the reconstruction efficiency of  $\Lambda_c^+ \rightarrow pK^-\pi^+$  decay;  $N_{pK^-\pi^+}^{\text{obs}} = (1281910 \pm 2040)$  represents the observed  $\Lambda_c^+ \rightarrow pK^-\pi^+$  signal

events in data; the branching fractions  $\mathcal{B}(\Lambda_c^+ \rightarrow \Sigma^+\pi^0)$ ,  $\mathcal{B}(\Lambda_c^+ \rightarrow \Sigma^+\eta)$ ,  $\mathcal{B}(\Lambda_c^+ \rightarrow pK^-\pi^+)$ ,  $\mathcal{B}(\Sigma^+ \rightarrow p\pi^0)$ ,  $\mathcal{B}(\pi^0 \rightarrow \gamma\gamma)$ , and  $\mathcal{B}(\eta \rightarrow \gamma\gamma)$  are taken from the Particle Data Group (PDG) [24]. Using the values above, the peaking background events from the contributions of  $\Lambda_c^+ \rightarrow \Sigma^+\pi^0(\rightarrow \gamma\gamma)$  and  $\Lambda_c^+ \rightarrow \Sigma^+\eta(\rightarrow \gamma\gamma)$  in the  $M(\Sigma^+\gamma)$  distribution are determined to be  $N_{\Sigma^+\pi^0}^{\Sigma^+\gamma} = (3617 \pm 344)$  and  $N_{\Sigma^+\eta}^{\Sigma^+\gamma} = (649 \pm 297)$ , respectively, where the uncertainties are mainly from the input branching fractions.

For the  $\Xi_c^0 \rightarrow \Xi^0\gamma$  mode, the corresponding backgrounds can not be estimated using this method, because the branching fractions of  $\Xi_c^0 \rightarrow \Xi^0\pi^0$  and  $\Xi_c^0 \rightarrow \Xi^0\eta$  decays have not yet been measured. To estimate the numbers of peaking background events from the contributions of  $\Xi_c^0 \rightarrow \Xi^0\pi^0(\rightarrow \gamma\gamma)$  and  $\Xi_c^0 \rightarrow \Xi^0\eta(\rightarrow \gamma\gamma)$  in the  $M(\Xi^0\gamma)$  distribution, we study the background channels  $\Xi_c^0 \rightarrow \Xi^0\pi^0$  and  $\Xi^0\eta$  in data. The  $\Xi^0$  candidates are selected using the same criteria used for the signal mode  $\Xi_c^0 \rightarrow \Xi^0\gamma$ . The  $\pi^0$  ( $\eta$ ) candidates are reconstructed from two photons having energy exceeding 110 MeV (230 MeV) in both barrel and endcaps of the ECL, and are required to have momentum exceeding 800 MeV/c (900 MeV/c) in the laboratory frame. Mass-constrained fits are performed for  $\pi^0$  and  $\eta$  candidates with a requirement of  $\chi^2 < 5$ . For  $\eta \rightarrow \gamma\gamma$  reconstruction,  $\mathcal{P}(\pi^0) < 0.6$  is required. The  $\Xi^0\pi^0$  and  $\Xi^0\eta$  combinations are then made to form  $\Xi_c^0$  candidates, and the scaled momentum  $x_p > 0.55$  is required.

After applying the event selection criteria above, the invariant mass spectra of  $\Xi^0\pi^0$  and  $\Xi^0\eta$  in data are shown in Figs. 6(a) and 6(b), respectively. The cyan shaded histograms represent events from the normalized  $\Xi^0$  sidebands, where the defined sideband regions of  $\Xi^0$  are the same as those of the signal channel. We observe significant  $\Xi_c^0 \rightarrow \Xi^0\pi^0(\rightarrow \gamma\gamma)$  and  $\Xi_c^0 \rightarrow \Xi^0\eta(\rightarrow \gamma\gamma)$

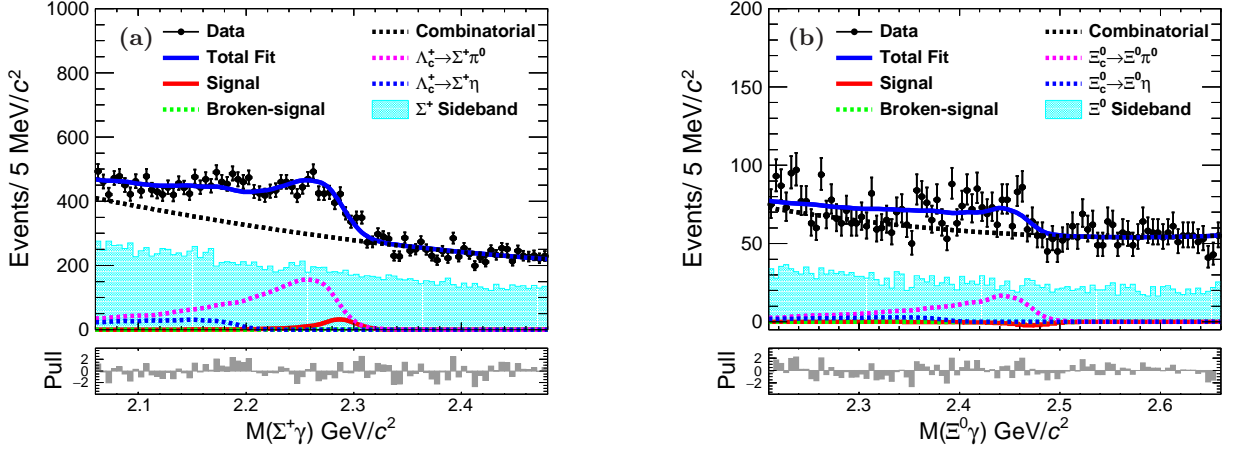


FIG. 5: The invariant mass distributions of (a)  $\Sigma^+\gamma$  and (b)  $\Xi^0\gamma$  from the reconstructed  $\Lambda_c^+ \rightarrow \Sigma^+\gamma$  and  $\Xi_c^0 \rightarrow \Xi^0\gamma$  candidates in data. The points with error bars represent the data, and the cyan shaded histograms denote events from the normalized  $\Sigma^+$  and  $\Xi^0$  sidebands. The blue solid curves show the best-fit results. The red solid and green dashed curves indicate the fitted signal and broken-signal components. The black dashed curves are the fitted combinatorial backgrounds. The pink and blue dashed curves show the fitted peaking backgrounds from the contributions of  $\Lambda_c^+ \rightarrow \Sigma^+\pi^0(\rightarrow \gamma\gamma)/\Xi_c^0 \rightarrow \Xi^0\pi^0(\rightarrow \gamma\gamma)$  and  $\Lambda_c^+ \rightarrow \Sigma^+\eta(\rightarrow \gamma\gamma)/\Xi_c^0 \rightarrow \Xi^0\eta(\rightarrow \gamma\gamma)$ , respectively.

signals in data, and no evident peaking backgrounds are found in the normalized  $\Xi^0$  sidebands or in the inclusive MC samples. To extract the  $\Xi_c^0$  signal yields from the  $\Xi_c^0 \rightarrow \Xi^0\pi^0(\rightarrow \gamma\gamma)$  and  $\Xi_c^0 \rightarrow \Xi^0\eta(\rightarrow \gamma\gamma)$  decays, we perform unbinned extended maximum-likelihood fits to the  $M(\Xi^0\pi^0)$  and  $M(\Xi^0\eta)$  distributions. The likelihood function includes the following components: (1) The signal PDF of  $\Xi_c^0$  candidates. (2) The broken-signal PDF from true  $\Xi_c^0 \rightarrow \Xi^0\pi^0(\rightarrow \gamma\gamma)$  or  $\Xi_c^0 \rightarrow \Xi^0\eta(\rightarrow \gamma\gamma)$  signal decays, where at least one of the final state particle candidates is wrongly assigned in reconstruction. (3) The combinatorial background PDF. A Crystal-Ball (CB) function [32] is taken as the  $\Xi_c^0$  signal PDF, the broken-signal is represented by a non-parametric (multi-dimensional) kernel estimation PDF [33] based on the signal MC simulation, and the combinatorial background PDF is described by a first-order polynomial. The parameters of signal and background PDFs are free. The ratios of signal to broken-signal components are fixed to (83.0%:17.0%) and (81.2%:18.8%) for  $\Xi_c^0 \rightarrow \Xi^0\pi^0(\rightarrow \gamma\gamma)$  and  $\Xi_c^0 \rightarrow \Xi^0\eta(\rightarrow \gamma\gamma)$ , respectively, according to the signal MC simulations. Hereinafter, the broken-signal component is regarded as part of the signal. Figure 6 displays the fit results along with the pull distributions. The fitted  $\Xi_c^0 \rightarrow \Xi^0\pi^0(\rightarrow \gamma\gamma)$  and  $\Xi_c^0 \rightarrow \Xi^0\eta(\rightarrow \gamma\gamma)$  signal yields in data are  $(1940 \pm 78)$  and  $(288 \pm 33)$ , respectively.

The peaking background events from the contributions of  $\Xi_c^0 \rightarrow \Xi^0\pi^0(\rightarrow \gamma\gamma)$  and  $\Xi_c^0 \rightarrow \Xi^0\eta(\rightarrow \gamma\gamma)$  in the  $M(\Xi^0\gamma)$  distribution are estimated from the following formulae

$$N_{\Xi^0\gamma}^{\Xi^0\pi^0} = \frac{N_{\Xi^0\pi^0}}{\epsilon_{\Xi^0\pi^0}} \times \epsilon_{\Xi^0\pi^0}^{\Xi^0\gamma}$$

and

$$N_{\Xi^0\gamma}^{\Xi^0\eta} = \frac{N_{\Xi^0\eta}}{\epsilon_{\Xi^0\eta}} \times \epsilon_{\Xi^0\eta}^{\Xi^0\gamma}.$$

Here,  $N_{\Xi^0\pi^0} = (1940 \pm 78)$  and  $N_{\Xi^0\eta} = (288 \pm 33)$  are the observed  $\Xi_c^0 \rightarrow \Xi^0\pi^0(\rightarrow \gamma\gamma)$  and  $\Xi_c^0 \rightarrow \Xi^0\eta(\rightarrow \gamma\gamma)$  signal events under  $\Xi_c^0 \rightarrow \Xi^0\pi^0(\rightarrow \gamma\gamma)$  and  $\Xi_c^0 \rightarrow \Xi^0\eta(\rightarrow \gamma\gamma)$  selection criteria in data with reconstruction efficiencies of  $\epsilon_{\Xi^0\pi^0} = (2.14 \pm 0.01)\%$  and  $\epsilon_{\Xi^0\eta} = (2.61 \pm 0.01)\%$ , respectively;  $\epsilon_{\Xi^0\pi^0}^{\Xi^0\gamma} = (0.35 \pm 0.01)\%$  and  $\epsilon_{\Xi^0\eta}^{\Xi^0\gamma} = (0.56 \pm 0.01)\%$  are the reconstruction efficiencies of  $\Xi_c^0 \rightarrow \Xi^0\pi^0(\rightarrow \gamma\gamma)$  and  $\Xi_c^0 \rightarrow \Xi^0\eta(\rightarrow \gamma\gamma)$  under  $\Xi_c^0 \rightarrow \Xi^0\gamma$  selection criteria, respectively. Using the values above, the peaking background events from the contributions of  $\Xi_c^0 \rightarrow \Xi^0\pi^0(\rightarrow \gamma\gamma)$  and  $\Xi_c^0 \rightarrow \Xi^0\eta(\rightarrow \gamma\gamma)$  in the  $M(\Xi^0\gamma)$  distribution are determined to be  $N_{\Xi^0\gamma}^{\Xi^0\pi^0} = (317 \pm 13)$  and  $N_{\Xi^0\gamma}^{\Xi^0\eta} = (62 \pm 7)$ , respectively, where the uncertainties are statistical only.

To extract the signal yields of  $\Lambda_c^+ \rightarrow \Sigma^+\gamma$  and  $\Xi_c^0 \rightarrow \Xi^0\gamma$  decays, we perform unbinned extended maximum-likelihood fits to  $M(\Sigma^+\gamma)$  and  $M(\Xi^0\gamma)$  distributions in Fig. 5, and the following components are included in the fits: (1) The signal PDF ( $\mathcal{F}_S$ ) of  $\Lambda_c^+$  or  $\Xi_c^0$  candidates. (2) The broken-signal PDF ( $\mathcal{F}_{BS}$ ) from the true  $\Lambda_c^+ \rightarrow \Sigma^+\gamma$  or  $\Xi_c^0 \rightarrow \Xi^0\gamma$  signal decay, where at least one of the final state particle candidates is wrongly assigned in reconstruction. (3) The peaking background PDFs ( $\mathcal{F}_{\pi^0}$  and  $\mathcal{F}_\eta$ ) from the contributions of  $\Lambda_c^+ \rightarrow \Sigma^+\pi^0(\rightarrow \gamma\gamma)/\Xi_c^0 \rightarrow \Xi^0\pi^0(\rightarrow \gamma\gamma)$  and  $\Lambda_c^+ \rightarrow \Sigma^+\eta(\rightarrow \gamma\gamma)/\Xi_c^0 \rightarrow \Xi^0\eta(\rightarrow \gamma\gamma)$ . (4) Other combinatorial background PDF

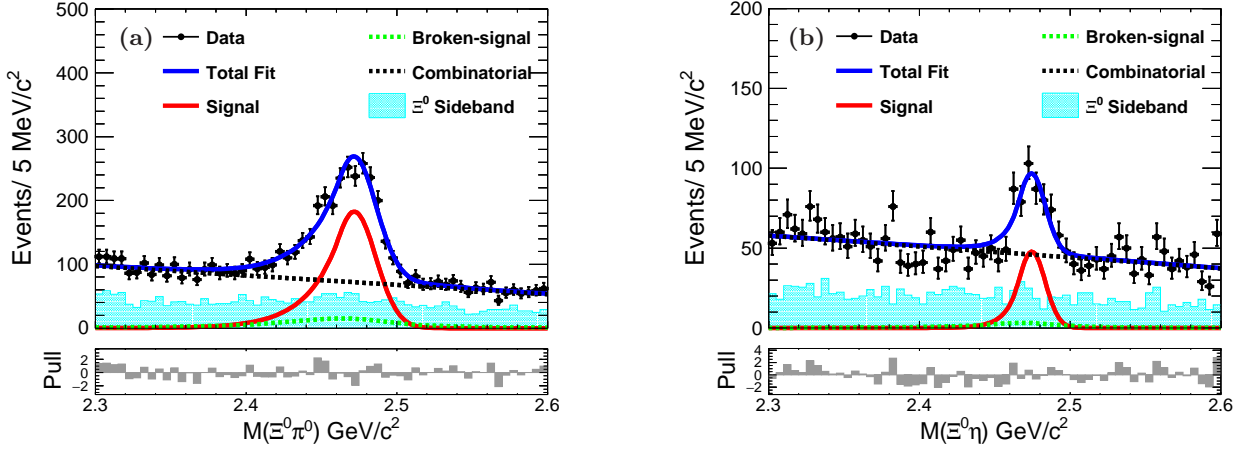


FIG. 6: The invariant mass distributions of (a)  $\Xi^0\pi^0$  and (b)  $\Xi^0\eta$  from reconstructed  $\Xi_c^0 \rightarrow \Xi^0\pi^0(\rightarrow\gamma\gamma)$  and  $\Xi_c^0 \rightarrow \Xi^0\eta(\rightarrow\gamma\gamma)$  candidates in data. The points with error bars represent the data, and the cyan shaded histograms denote events from the normalized  $\Xi^0$  sidebands. The blue solid curves show the best-fit results. The red solid and green dashed curves indicate the fitted signal and broken-signal components. The black dashed curves are the fitted combinatorial backgrounds.

( $\mathcal{F}_B$ ). The likelihood function is defined as

$$\mathcal{L} = \frac{e^{-(n_S+n_{B_1}+n_{B_2})}}{N!} \prod_i^N \{n_S[f_S\mathcal{F}_S(M_i) + (1-f_S)\mathcal{F}_{BS}(M_i)] + n_{B_1}[f_{B_1}\mathcal{F}_{\pi^0}(M_i) + (1-f_{B_1})\mathcal{F}_\eta(M_i)] + n_{B_2}\mathcal{F}_B(M_i)\},$$

where  $N$  is the total number of observed events;  $n_S$ ,  $n_{B_1}$ , and  $n_{B_2}$  are the total numbers of signal events (the broken-signal is regarded as part of the signal), the peaking background events, and other combinatorial background events, respectively;  $f_S$  and  $f_{B_1}$  indicate the fractions of the correctly reconstructed signal events in the total number of signal events and the peaking background events from  $\Lambda_c^+ \rightarrow \Sigma^+\pi^0(\rightarrow\gamma\gamma)$  or  $\Xi_c^0 \rightarrow \Xi^0\pi^0(\rightarrow\gamma\gamma)$  in the total number of peaking background events, respectively;  $M$  represents the  $\Sigma^+\gamma$  or  $\Xi^0\gamma$  invariant mass;  $i$  denotes the event index. The signal PDF is parameterized by a CB function [32], and the parameters of the signal PDF are fixed to those obtained from signal MC simulation. The broken-signal and the peaking background are represented by non-parametric (multi-dimensional) kernel estimation PDFs [33] based on signal MC simulations. The other combinatorial background PDF is a second-order polynomial. The values of  $n_S$ ,  $n_{B_1}$ , and  $n_{B_2}$  are free in the fit. The ratios of signal to broken-signal components are fixed to (91.3%:8.7%) and (84.7%:15.3%) for  $\Lambda_c^+ \rightarrow \Sigma^+\gamma$  and  $\Xi_c^0 \rightarrow \Xi^0\gamma$ , respectively, according to the signal MC simulations. Since the shapes of the two peaking background components cannot be separated well, the ratios of peaking background events from  $\Lambda_c^+ \rightarrow \Sigma^+\pi^0(\rightarrow\gamma\gamma)$  relative to those from  $\Lambda_c^+ \rightarrow \Sigma^+\eta(\rightarrow\gamma\gamma)$  and peaking background events from  $\Xi_c^0 \rightarrow \Xi^0\pi^0(\rightarrow\gamma\gamma)$  relative to those from  $\Xi_c^0 \rightarrow \Xi^0\eta(\rightarrow\gamma\gamma)$  are fixed to (84.8%:15.2%) and (83.6%:16.4%), respectively, based

on the expected events in the  $M(\Sigma^+\gamma)$  and  $M(\Xi^0\gamma)$  distributions in data. The fitted results are displayed in Fig. 5 along with the pull distributions, and the fitted signal yields of  $\Lambda_c^+ \rightarrow \Sigma^+\gamma$  and  $\Xi_c^0 \rightarrow \Xi^0\gamma$  decays in data are  $(340 \pm 110)$  and  $(-18 \pm 48)$ , respectively. The fitted numbers of peaking background events are consistent with the corresponding expected numbers of events within the ranges of uncertainties. The statistical significance of the  $\Lambda_c^+ \rightarrow \Sigma^+\gamma$  decay is  $3.2\sigma$  calculated using  $\sqrt{-2\ln(\mathcal{L}_0/\mathcal{L}_{\max})}$ , where  $\mathcal{L}_0$  and  $\mathcal{L}_{\max}$  are the likelihoods of the fits without and with signal and broken-signal components, respectively. To estimate the signal significance of  $\Lambda_c^+ \rightarrow \Sigma^+\gamma$  decay after considering the systematic uncertainties, several alternative fits discussed in the section of systematic uncertainty to the  $M(\Sigma^+\gamma)$  spectrum are performed. The signal significance of  $\Lambda_c^+ \rightarrow \Sigma^+\gamma$  decay is larger than  $2.2\sigma$  in all cases. We take  $2.2\sigma$  as the signal significance with systematic uncertainties included.

## V. SYSTEMATIC UNCERTAINTIES

The systematic uncertainties on the measurements of branching fraction ratios can be divided into two categories as discussed below.

The sources of multiplicative systematic uncertainties include detection-efficiency-related uncertainties, the modeling of MC event generation, and branching fractions of intermediate states. Note that the uncertainties from detection-efficiency-related sources partially cancel in the ratio to the normalization channel.

The detection-efficiency-related uncertainties include those from tracking efficiency, PID efficiency,  $\pi^0$

reconstruction efficiency, and photon reconstruction efficiency. Based on a study of  $D^{*+} \rightarrow \pi^+ D^0 (\rightarrow K_S^0 \pi^+ \pi^-)$  decay, the tracking efficiency uncertainty is evaluated to be 0.35% per track. Using  $D^{*+} \rightarrow D^0 \pi^+$ ,  $D^0 \rightarrow K^- \pi^+$ , and  $\Lambda \rightarrow p \pi^-$  control samples, the PID efficiency uncertainties are estimated to be 0.95% per kaon and 0.96% per pion for the normalization channel  $\Lambda_c^+ \rightarrow p K^- \pi^+$ . For the normalization channel  $\Xi_c^0 \rightarrow \Xi^- (\rightarrow \Lambda \pi^-) \pi^+$ , the PID efficiency uncertainties of  $\pi^+$  from the  $\Xi_c^0$  decay and  $\pi^-$  from the  $\Xi^-$  decay are considered separately, because the  $\pi^+$  has a higher momentum. The PID efficiency ratio between the data and MC simulation of  $\pi^+$  is found to be  $\epsilon_{\text{data}}/\epsilon_{\text{MC}} = (95.4 \pm 0.7)\%$ , so we take 95.4% and 0.7% as the efficiency correction factor and PID uncertainty for  $\pi^+$ ; the PID efficiency ratio between the data and MC simulation of  $\pi^-$  is found to be  $\epsilon_{\text{data}}/\epsilon_{\text{MC}} = (99.5 \pm 0.8)\%$ , and 1.3% is taken as the PID uncertainty of  $\pi^-$ . The uncertainties from proton PID efficiency and  $\Lambda$  reconstruction mostly cancel in the ratio with the normalization channel. The PID uncertainties of  $K$  and  $\pi$  are added linearly to obtain the final PID uncertainties, which are 1.9% and 2.0% for the measurements of  $\mathcal{B}(\Lambda_c^+ \rightarrow \Sigma^+ \gamma)/\mathcal{B}(\Lambda_c^+ \rightarrow p K^- \pi^+)$  and  $\mathcal{B}(\Xi_c^0 \rightarrow \Xi^0 \gamma)/\mathcal{B}(\Xi_c^0 \rightarrow \Xi^- \pi^+)$ , respectively. The uncertainties associated with  $\pi^0$  and radiative photon reconstruction efficiencies are treated as independent, and are estimated to be 2.3% [34] and 2.0% [35], respectively. Assuming these uncertainties are independent and adding them in quadrature, the final detection-efficiency-related uncertainties are obtained, as listed in Table II.

We assume that both  $\Lambda_c^+ \rightarrow \Sigma^+ \gamma$  and  $\Xi_c^0 \rightarrow \Xi^0 \gamma$  decays are isotropic in the rest frame of the parent particle, and a phase space model is used to generate signal events by default. Alternative angular distributions ( $1 \pm \cos^2 \theta_\gamma$ ) are also generated, where  $\theta_\gamma$  is the angle between the  $\gamma$  momentum vector and the boost direction from the laboratory frame in the  $\Lambda_c^+$  or  $\Xi_c^0$  C.M. frame. The maximum differences in the reconstruction efficiencies between the alternatives and default signal MC samples are taken as systematic uncertainties, which are 6.9% and 2.3% for  $\Lambda_c^+ \rightarrow \Sigma^+ \gamma$  and  $\Xi_c^0 \rightarrow \Xi^0 \gamma$ , respectively.

For the measurement of  $\mathcal{B}(\Lambda_c^+ \rightarrow \Sigma^+ \gamma)/\mathcal{B}(\Lambda_c^+ \rightarrow p K^- \pi^+)$ , the uncertainties from  $\mathcal{B}(\Sigma^+ \rightarrow p \pi^0)$  and  $\mathcal{B}(\pi^0 \rightarrow \gamma \gamma)$  are 0.6% and 0.035% [24], which are added in quadrature as the total uncertainty from branching fractions of intermediate states. For the measurement of  $\mathcal{B}(\Xi_c^0 \rightarrow \Xi^0 \gamma)/\mathcal{B}(\Xi_c^0 \rightarrow \Xi^- \pi^+)$ , the uncertainties from  $\mathcal{B}(\Xi^- \rightarrow \Lambda \pi^-)$ ,  $\mathcal{B}(\Xi^0 \rightarrow \Lambda \pi^0)$ , and  $\mathcal{B}(\pi^0 \rightarrow \gamma \gamma)$  are 0.035%, 0.012%, and 0.035% [24], which are added in quadrature as the total uncertainty from branching fractions of intermediate states.

Additive systematic uncertainties associated with the combinatorial background PDF, fit range,  $\Lambda_c^+$  or  $\Xi_c^0$  mass resolution, the ratio of the signal component to the broken-signal component, and the peaking backgrounds

from the contributions of  $\Lambda_c^+ \rightarrow \Sigma^+ \pi^0 (\rightarrow \gamma \gamma)/\Xi_c^0 \rightarrow \Xi^0 \pi^0 (\rightarrow \gamma \gamma)$  and  $\Lambda_c^+ \rightarrow \Sigma^+ \eta (\rightarrow \gamma \gamma)/\Xi_c^0 \rightarrow \Xi^0 \eta (\rightarrow \gamma \gamma)$  are considered as follows: (1) The combinatorial background PDF is replaced by a higher- or lower-order polynomial. (2) The fit range is changed by  $\pm 30$  MeV/ $c^2$ . (3) To consider the uncertainty associated with  $\Lambda_c^+$  or  $\Xi_c^0$  mass resolution, the signal PDF of  $\Lambda_c^+$  or  $\Xi_c^0$  is replaced by a Gaussian function with free resolution convolved with the fixed signal shape from signal MC simulation. (4) Since the ratio of the signal component to the broken-signal component in signal MC simulation may not be consistent with that in data, we add an extra broken-signal component described by the same PDF as original broken-signal with free yield to fit the data. (5) The number of peaking background events from the contributions of  $\Lambda_c^+ \rightarrow \Sigma^+ \pi^0/\Xi_c^0 \rightarrow \Xi^0 \pi^0$  and  $\Lambda_c^+ \rightarrow \Sigma^+ \eta/\Xi_c^0 \rightarrow \Xi^0 \eta$  is constrained with a Gaussian function whose mean value and width are equal to the number of expected events in  $M(\Sigma^+ \gamma)$  or  $M(\Xi^0 \gamma)$  distribution and the corresponding uncertainty. For the normalization channels  $\Lambda_c^+ \rightarrow p K^- \pi^+$  and  $\Xi_c^0 \rightarrow \Xi^- \pi^+$ , the additive systematic uncertainties associated with the background PDF and fit range are estimated using the same method as above, and then summed in quadrature to obtain the total additive systematic uncertainties, which are 1.9% and 3.1% for  $\Lambda_c^+ \rightarrow p K^- \pi^+$  and  $\Xi_c^0 \rightarrow \Xi^- \pi^+$ , respectively.

Since no evident  $\Lambda_c^+ \rightarrow \Sigma^+ \gamma$  or  $\Xi_c^0 \rightarrow \Xi^0 \gamma$  signals are found, the upper limits on the numbers of signal events ( $N^{\text{UL}}$ ) at 90% credibility level (C.L.) are determined by solving the equation

$$\int_0^{N^{\text{UL}}} \mathcal{L}(N) dN / \int_0^{+\infty} \mathcal{L}(N) dN = 0.9,$$

where  $N$  represents the assumed  $\Lambda_c^+ \rightarrow \Sigma^+ \gamma$  or  $\Xi_c^0 \rightarrow \Xi^0 \gamma$  signal events and the  $\mathcal{L}(N)$  is the corresponding maximized likelihood of the fit to the assumption, and the systematic uncertainties are taken into account in two steps. First, when we study the additive systematic uncertainties described above, we calculate the upper limit for each possible case, and take the most conservative upper limit at 90% C.L. on the number of signal events. For the  $\Lambda_c^+ \rightarrow \Sigma^+ \gamma$  decay, when the combinatorial background PDF is replaced by a third-order polynomial, the fit range is reduced by 30 MeV/ $c^2$ , and the signal PDF of  $\Lambda_c^+$  is replaced by a Gaussian function with free resolution convolved with the fixed signal shape, the obtained upper limit is the most conservative. For the  $\Xi_c^0 \rightarrow \Xi^0 \gamma$  decay, when the fit range is reduced by 30 MeV/ $c^2$ , the signal PDF of  $\Xi_c^0$  is replaced by a Gaussian function with free resolution convolved with the fixed signal shape, and the number of peaking background events is constrained with a Gaussian function, the obtained upper limit is the most conservative. Then, the multiplicative systematic uncertainties from the signal and normalization channels and the additive systematic



uncertainty from the normalization channel are summed in quadrature to give the total systematic uncertainty, and the likelihood with the most conservative upper limit is convolved with a Gaussian function whose width is equal to the corresponding total systematic uncertainty. Furthermore, to obtain the upper limits on the absolute branching fractions  $\mathcal{B}(\Lambda_c^+ \rightarrow \Sigma^+\gamma)$  and  $\mathcal{B}(\Xi_c^0 \rightarrow \Xi^0\gamma)$  at 90% C.L., the multiplicative systematic uncertainties from the signal and normalization channels, the additive systematic uncertainty from the normalization channel, and the uncertainty from branching fraction  $\mathcal{B}(\Lambda_c^+ \rightarrow pK^-\pi^+)$  or  $\mathcal{B}(\Xi_c^0 \rightarrow \Xi^-\pi^+)$  are added in quadrature as total systematic uncertainty, and then the likelihood with the most conservative upper limit is convolved with a Gaussian function whose width equals to the corresponding total systematic uncertainty.

Assuming all the sources are independent and adding the multiplicative systematic uncertainties and additive systematic uncertainties from normalization channel in quadrature, the total systematic uncertainties are obtained. All the systematic uncertainties are summarized in Table II.

TABLE II: Relative systematic uncertainties (%) on the measurements of branching fraction ratios  $\mathcal{B}(\Lambda_c^+ \rightarrow \Sigma^+\gamma)/\mathcal{B}(\Lambda_c^+ \rightarrow pK^-\pi^+)$  and  $\mathcal{B}(\Xi_c^0 \rightarrow \Xi^0\gamma)/\mathcal{B}(\Xi_c^0 \rightarrow \Xi^-\pi^+)$ .

Sources	$\frac{\mathcal{B}(\Lambda_c^+ \rightarrow \Sigma^+\gamma)}{\mathcal{B}(\Lambda_c^+ \rightarrow pK^-\pi^+)}$	$\frac{\mathcal{B}(\Xi_c^0 \rightarrow \Xi^0\gamma)}{\mathcal{B}(\Xi_c^0 \rightarrow \Xi^-\pi^+)}$
Detection efficiency	3.7	3.7
Branching fraction	0.6	0.1
The modeling of MC events	6.9	2.3
Additive uncertainty	1.9	3.1
Sum	8.1	5.4

## VI. CALCULATIONS OF THE RATIOS OF BRANCHING FRACTIONS

The most conservative upper limits on the numbers of  $\Lambda_c^+ \rightarrow \Sigma^+\gamma$  and  $\Xi_c^0 \rightarrow \Xi^0\gamma$  signal events at 90% C.L. are determined to be 608 and 91, respectively, and then the upper limits at 90% C.L. on the ratios of the branching fractions are determined from the following formulae

$$\begin{aligned} \frac{\mathcal{B}(\Lambda_c^+ \rightarrow \Sigma^+\gamma)}{\mathcal{B}(\Lambda_c^+ \rightarrow pK^-\pi^+)} &< \frac{N_{\Sigma^+\gamma}^{\text{UL}} \epsilon_{pK^-\pi^+}}{N_{pK^-\pi^+}^{\text{obs}} \epsilon_{\Sigma^+\gamma}} \\ &\times \frac{1}{\mathcal{B}(\Sigma^+ \rightarrow p\pi^0)\mathcal{B}(\pi^0 \rightarrow \gamma\gamma)} \\ &= 4.0 \times 10^{-3} \end{aligned}$$

and

$$\begin{aligned} \frac{\mathcal{B}(\Xi_c^0 \rightarrow \Xi^0\gamma)}{\mathcal{B}(\Xi_c^0 \rightarrow \Xi^-\pi^+)} &< \frac{N_{\Xi^0\gamma}^{\text{UL}} \epsilon_{\Xi^-\pi^+}}{N_{\Xi^-\pi^+}^{\text{obs}} \epsilon_{\Xi^0\gamma}} \\ &\times \frac{\mathcal{B}(\Xi^- \rightarrow \Lambda\pi^-)}{\mathcal{B}(\Xi^0 \rightarrow \Lambda\pi^0)\mathcal{B}(\pi^0 \rightarrow \gamma\gamma)} \\ &= 1.2 \times 10^{-2}. \end{aligned}$$

Here  $N_{\Sigma^+\gamma}^{\text{UL}}$  and  $N_{\Xi^0\gamma}^{\text{UL}}$  represent the upper limits on the numbers of  $\Lambda_c^+ \rightarrow \Sigma^+\gamma$  and  $\Xi_c^0 \rightarrow \Xi^0\gamma$  signal events at 90% C.L.;  $N_{pK^-\pi^+}^{\text{obs}}$  and  $N_{\Xi^-\pi^+}^{\text{obs}}$  denote the observed signal events of  $\Lambda_c^+ \rightarrow pK^-\pi^+$  and  $\Xi_c^0 \rightarrow \Xi^-\pi^+$  decays in data;  $\epsilon_{\Sigma^+\gamma}$ ,  $\epsilon_{\Xi^0\gamma}$ ,  $\epsilon_{pK^-\pi^+}$ , and  $\epsilon_{\Xi^-\pi^+}$  are the corresponding reconstruction efficiencies, which are obtained from the signal MC simulations and are listed in Table III; the branching fractions  $\mathcal{B}(\Sigma^+ \rightarrow p\pi^0) = (51.57 \pm 0.03)\%$ ,  $\mathcal{B}(\pi^0 \rightarrow \gamma\gamma) = (98.823 \pm 0.034)\%$ ,  $\mathcal{B}(\Xi^- \rightarrow \Lambda\pi^-) = (99.887 \pm 0.035)\%$ , and  $\mathcal{B}(\Xi^0 \rightarrow \Lambda\pi^0) = (99.524 \pm 0.012)\%$  are taken from the PDG [24]. Since the statistical significance of  $\Lambda_c^+ \rightarrow \Sigma^+\gamma$  is  $3.2\sigma$ , we also give the ratio of branching fractions with  $N_{\Sigma^+\gamma}^{\text{obs}} = (340 \pm 110)$  replacing  $N_{\Sigma^+\gamma}^{\text{UL}}$  in above formula,  $\mathcal{B}(\Lambda_c^+ \rightarrow \Sigma^+\gamma)/\mathcal{B}(\Lambda_c^+ \rightarrow pK^-\pi^+) = (2.23 \pm 0.72 \pm 0.63) \times 10^{-3}$ , where the first uncertainty is statistical, and the second one arises from the multiplicative and additive systematic uncertainties discussed in Sec. V.

TABLE III: Summary of the fitted signal events ( $N^{\text{obs}}$ ), the upper limits at 90% C.L. on the numbers of signal events ( $N^{\text{UL}}$ ), and the reconstruction efficiencies ( $\epsilon$ ). All the uncertainties here are statistical only.

Modes	$N^{\text{obs}}$	$N^{\text{UL}}$	$\epsilon(\%)$
$\Lambda_c^+ \rightarrow \Sigma^+\gamma$	$340 \pm 110$	608	$2.98 \pm 0.01$
$\Xi_c^0 \rightarrow \Xi^0\gamma$	$-18 \pm 48$	91	$3.03 \pm 0.01$
$\Lambda_c^+ \rightarrow pK^-\pi^+$	$1281910 \pm 2040$	...	$12.79 \pm 0.02$
$\Xi_c^0 \rightarrow \Xi^-\pi^+$	$45063 \pm 445$	...	$16.96 \pm 0.05$

## VII. SUMMARY

In summary, using the entire data sample of  $980 \text{ fb}^{-1}$  integrated luminosity collected by the Belle detector, we perform the first search for the weak radiative decays  $\Lambda_c^+ \rightarrow \Sigma^+\gamma$  and  $\Xi_c^0 \rightarrow \Xi^0\gamma$ . No evidences for  $\Lambda_c^+ \rightarrow \Sigma^+\gamma$  or  $\Xi_c^0 \rightarrow \Xi^0\gamma$  signals are found. The upper limits at 90% C.L. on the ratios of the branching fractions

$$\frac{\mathcal{B}(\Lambda_c^+ \rightarrow \Sigma^+\gamma)}{\mathcal{B}(\Lambda_c^+ \rightarrow pK^-\pi^+)} < 4.0 \times 10^{-3}$$

and

$$\frac{\mathcal{B}(\Xi_c^0 \rightarrow \Xi^0\gamma)}{\mathcal{B}(\Xi_c^0 \rightarrow \Xi^-\pi^+)} < 1.2 \times 10^{-2}$$

are measured. Taking  $\mathcal{B}(\Lambda_c^+ \rightarrow pK^-\pi^+) = (6.28 \pm 0.32)\%$  and  $\mathcal{B}(\Xi_c^0 \rightarrow \Xi^-\pi^+) = (1.43 \pm 0.32)\%$ , we determine the upper limits at 90% C.L. on the absolute branching fractions  $\mathcal{B}(\Lambda_c^+ \rightarrow \Sigma^+\gamma) < 2.6 \times 10^{-4}$  and  $\mathcal{B}(\Xi_c^0 \rightarrow \Xi^0\gamma) < 1.8 \times 10^{-4}$ . The measured upper limits on the absolute branching fractions of  $\Lambda_c^+ \rightarrow \Sigma^+\gamma$  and  $\Xi_c^0 \rightarrow \Xi^0\gamma$  are slightly smaller than the

theoretical predictions of case (II) in Ref. [5], which naively considered the flavor dependence of charmed baryon wave-function squared at the origin  $|\psi(0)|^2$ .

We thank the KEKB group for the excellent operation of the accelerator; the KEK cryogenics group for the efficient operation of the solenoid.

- 
- [1] G. Burdman, E. Golowich, J. L. Hewett, and S. Pakvasa, Phys. Rev. D **52**, 6383 (1995).
- [2] C. Greub, T. Hurth, M. Misiak, and D. Wyler, Phys. Lett. B **382**, 415 (1996).
- [3] S. Fajfer and P. Singer, Phys. Rev. D **56**, 4302 (1997).
- [4] A. N. Kamal, Phys. Rev. D **28**, 2176 (1983).
- [5] T. Uppal and R. C. Verma, Phys. Rev. D **47**, 2858 (1993).
- [6] H. Y. Cheng, C. Y. Cheung, G. L. Lin, Y. C. Lin, T. M. Yan, and H. L. Yu, Phys. Rev. D **51**, 1199 (1995).
- [7] B. Bajc, S. Fajfer, and R. J. Oakes, Phys. Rev. D **51**, 2230 (1995).
- [8] S. Fajfer, arXiv:1509.01997.
- [9] O. Tajima *et al.* (Belle Collaboration), Phys. Rev. Lett. **92**, 101803 (2004).
- [10] B. Aubert *et al.* (BABAR Collaboration), Phys. Rev. D **78**, 071101 (2008).
- [11] T. Nanut *et al.* (Belle Collaboration), Phys. Rev. Lett. **118**, 051801 (2017).
- [12] R. Aaij *et al.* (LHCb Collaboration), Phys. Rev. Lett. **123**, 031801 (2019).
- [13] H. Y. Cheng, arXiv:2109.01216.
- [14] N. Adolph and G. Hiller, Phys. Rev. D **105**, 116001 (2022).
- [15] A. Abashian *et al.* (Belle Collaboration), Nucl. Instrum. Methods Phys. Res., Sect. A **479**, 117 (2002).
- [16] J. Brodzicka *et al.*, Prog. Theor. Exp. Phys. **2012**, 04D001 (2012).
- [17] S. Kurokawa and E. Kikutani, Nucl. Instrum. Methods Phys. Res., Sect. A **499**, 1 (2003), and other papers included in this volume.
- [18] T. Abe *et al.*, Prog. Theor. Exp. Phys. **2013**, 03A001 (2013), and references therein.
- [19] D. J. Lange, Nucl. Instrum. Methods Phys. Res., Sect. A **462**, 152 (2001).
- [20] T. Sjöstrand, P. Edén, C. Friberg, L. Lönnblad, G. Miu, S. Mrenna, and E. Norrbin, Comput. Phys. Commun. **135**, 238 (2001).
- [21] R. Brun *et al.*, GEANT 3: user's guide Geant 3.10, Geant 3.11, CERN Report No. DD/EE/84-1, 1984.
- [22] G. Punzi, eConf **C030908**, MODT002 (2003).
- [23] E. Nakano, Nucl. Instrum. Methods Phys. Res., Sect. A **494**, 402 (2002).
- [24] P. A. Zyla *et al.* (Particle Data Group), Prog. Theor. Exp. Phys. **2020**, 083C01 (2020) and 2021 update.
- [25] J. Yelton *et al.* (Belle Collaboration), Phys. Rev. D **97**, 032001 (2018).
- [26] P. Koppenburg *et al.* (Belle Collaboration), Phys. Rev. Lett. **93**, 061803 (2004).
- [27] S. X. Li *et al.* (Belle Collaboration), J. High Energy Phys. **03**, 090 (2022).
- [28] S. Jia *et al.* (Belle Collaboration), J. High Energy Phys. **06**, 160 (2021).
- [29] K. Hanagaki, H. Kakuno, H. Ikeda, T. Iijima, and T. Tsukamoto, Nucl. Instrum. Methods Phys. Res., Sect. A **485**, 490 (2002).
- [30] R. H. Dalitz, Philos. Mag. Ser. 5 **44**, 1068 (1953).
- [31] X. Y. Zhou, S. X. Du, G. Li, and C. P. Shen, Comput. Phys. Commun. **258**, 107540 (2021).
- [32] J. E. Gaiser, Ph. D. thesis, Stanford Linear Accelerator Center, Stanford University, Report No. SLAC-R-255, 1982.
- [33] K. S. Cranmer, Comput. Phys. Commun. **136**, 198 (2001).
- [34] S. Ryu *et al.* (Belle Collaboration), Phys. Rev. D **89**, 072009 (2014).
- [35] T. Horiguchi *et al.* (Belle Collaboration), Phys. Rev. Lett. **119**, 191802 (2017).